AIMS Mathematics, 10(12): 28374–28395.
DOI: 10.3934/math.20251248
Received: 14 September 2025
Revised: 04 November 2025
Accepted: 24 November 2025
Published: 03 December 2025

https://www.aimspress.com/journal/Math

Research article

Traveling wave reductions and adaptive moving mesh computations for the improved Boussinesq equation

Amer Ahmed[1,2,*], **Taghread Ghannam Alharbi**[2], **A. R. Alharbi**[2] **and Ishak Hashim**[1,3]

[1] Department of Mathematical Sciences, Faculty of Science & Technology, Universiti Kebangsaan Malaysia, 43600 UKM Bangi, Selangor, Malaysia

[2] Department of Mathematics, College of Science, Taibah University, 42353, Medina, Saudi Arabia

[3] Nonlinear Dynamics Research Center (NDRC), Ajman University, Ajman, P.O. Box 346, United Arab Emirates

* **Correspondence:** Email: amer.abdulfattah.ahmed@gmail.com; Tel: +601118927524.

Abstract: This paper is concerned with the analytical and numerical study of the improved Boussinesq (IB) equation, a nonlinear dispersive model for applications in fluid dynamics, elasticity, geophysics, and nonlinear optics. Two systematic symbolic algorithms, i.e., the generalized tanh method and the $(1/\Theta')$-expansion method, are used for the recovery of analytical traveling-wave solutions of the IB equation. These solutions reveal a vast taxonomy of nonlinear waveforms corresponding to solitary, rational, and periodic profiles, governed by parameter combinations that regulate dispersion, wave amplitude, and phase. As a complement to the analytical study, we use an *r*-adaptive numerical method built from the Parabolic Monge-Ampère (PMA) moving mesh method and discretized by central differences in space and BDF2 in time. An adaptive algorithm automatically relocates the mesh nodes toward locations where sharp gradients are present, thereby ensuring accuracy and efficiency and preventing unnecessary computational cost. Numerical experiments evidence second-order convergence and stability and demonstrate the ability of the method to resolve sharp wave interaction without spurious oscillations. In total, the combination of exact benchmarks and adaptive simulation provides a practical framework for simulating nonlinear dispersive waves with impact in applications such as tsunami simulation, earthquake wave propagation, and optical signal pulse transmission.

Keywords: nonlinear wave dynamics; exact solutions; numerical solutions; generalized tanh method; adaptive moving mesh technique; soliton performance; wave interactions
Mathematics Subject Classification: 35A25, 35B35, 35Q51, 35Q92, 65M06, 65M12, 65M50

1. Introduction

Nonlinear wave propagation is a mathematical physics classic, with applications to liquid dynamics and plasma physics, elasticity, and nonlinear optics, to name just a few. In particular, these processes are normally modeled by nonlinear partial differential equations (NPDEs), which showcase a subtle balance between dispersion and nonlinearity. Among such models, the Boussinesq equation has had a pioneering role in describing shallow water dynamics ever since it was first postulated by Joseph Boussinesq in the nineteenth century [1–3]. Nevertheless, its classical version was cursed with instability for short wavelengths and was therefore commonly referred to as the "bad Boussinesq" equation. As a result, these unbounded growths of short-wave modes caused the model to fail in producing reliable simulations. Consequently, to overcome these shortcomings, modified versions were proposed, most notably its so-called "good" or improved version, which incorporates dispersive corrections to eliminate spurious short-wave growths [4–6].

In these analyses, our improved version of the Boussinesq equation of interest takes the version

$$\psi_{tt} - \mu\,\psi_{xxtt} - \kappa^2\psi_{xx} - \psi\,\psi_{xx} - (\psi_x)^2 = 0, \tag{1.1}$$

with dispersive parameter $\mu > 0$ and constant coefficient κ. The improved Boussinesq (IB) equation admits conserved quantities (e.g., energy and momentum); their explicit forms will be recalled in Section 2, which makes it a convenient setting for the analysis of nonlinear dispersive waves.

The IB model has found broad applicability in applied science and engineering. For instance, it can be applied in coastal hydrodynamics to model wave propagation of long surface wave motions over variable bathymetry with appropriate representation of such essential properties as shoaling, dispersion, and solitary wave interactions [7]. In addition, it has also found applications in modeling tsunami dynamics, wherein appropriate prediction of wave shape and wave velocity is of critical importance for the prediction of hazards [8]. In elasticity theory, its versions provide wave motions in elastic rods [9], while in geophysics, it provides a model of wave motions of seismic waves in layered media [10].

Beyond solid and fluid mechanics, the IB model is also found in nonlinear optics and transmission lines, where it serves to regulate the balance between dispersive and nonlinear forces that sustain soliton-like pulses [11, 12]. Notably, it plays a central role in designing light communication systems and artificial media, whose primary goal is to transmit signals with minimal distortion. Moreover, the diverse applications of the IB equation to these different problems highlight its importance and, as a result, continue to stimulate investigations on both exact analytical solutions and efficient schemes for its accurate simulation [13, 14].

An important feature of Eq (1.1) is its ability to accommodate solitonic solutions, brief waveforms forming out of a subtle interplay between nonlinearity and dispersion. Indeed, such solitons are of great importance because of their stability and robustness over significant distances. Consequently, emulating such dynamics is of qualitative importance to simulate real-world processes like propagation of tsunami waves and signal transmission in optical fibers [15, 16].

Several analytical approaches have been established over the past decades for finding highly accurate solutions of Boussinesq-type equations, including the tanh-function technique, the Jacobi elliptic expansions, the expansion scheme of $(1/\Theta')$, and the extended trial equation approach [17–20]. These approaches aid in understanding the shape and development of nonlinear waves but rely on

simplifying assumptions or idealized conditions and may diminish the range of application [21–23]. The IB equation, when numerically solved, poses considerable difficulties, necessitating accurate and stable numerical schemes. Classical schemes like finite difference [24], finite volume [25], and finite element schemes [26] have been thoroughly utiliszed with varying degrees of success.

In addition, more advanced schemes include meshless radial basis function collocation, operator splitting schemes [27], and adaptive moving mesh techniques [28, 29], such as the Parabolic Monge-Ampère (PMA) method, which dynamically relocates grid points to areas of sharp wave interactions or steep gradients [30, 31].

Within this context, the literature reports the following computational and convergence properties for r-adaptive PMA. Specifically, Domain Decomposition PMA shows a reduction in wall time with increasing resolutions, especially in three dimensions, where the Alternating DDPMA algorithm is faster than single-domain PMA as measured by timings [32]. In addition, spatial second-order convergence and temporal first-order convergence factors have been observed, and the Domain Decomposition solution converges towards the single-domain solution as a result of increasing iterations in the pseudo-time integration [32]. Furthermore, r-adaptive techniques are considered promising tools towards optimal redistribution; PMA schemes are simple to implement as a single scalar equation in any number of spatial dimensions [33].

Despite these developments, several challenges remain. On the one hand, analytic methods are typically restricted to smaller geometries or certain boundary conditions. Analytic methods provide closed-form travelling waves in specific settings; however, these methods are generally not applicable across all boundary types or parameter regimes [34, 35]. A common step in such reductions is the balancing principle, where the highest derivative term is balanced against the leading-order nonlinearity to determine the appropriate order of the ansatz [36,37]. Since different regimes are often distinguished by parameter features such as signs or discriminants, it is valuable to employ complementary solution templates. For instance, Riccati or tanh-type constructions are effective in certain parameter ranges, while linear-auxiliary expansions, such as the (G'/G) method or exponential forms like $\exp(-\Phi)$, capture different profiles and behaviors [38, 39].

On the other hand, schemes of a numerical sort often do not remain stable and precise for large-time simulations. In particular, for robust modeling of nonlinear wave interactions and stable solitary structures, schemes must not only converge and be stable but also adapt to characteristics of the evolving solution [40, 41]. Therefore, the present work addresses these challenges by amalgamating mutually reinforcing analytical and numerical approaches. Specifically, analytically, we combine the generalized tanh method and the $(1/\Theta')$-expansion technique to derive new classes of exact traveling-wave solutions of the IB equation. Moreover, numerically, we implement an implicit finite difference method with the adaptive PMA moving mesh algorithm. Finally, the analytical solutions serve to verify the stability, convergence, and reliability of the proposed schemes [42, 43].

The method of generalized tanh gives closed forms through a finite polynomial in some Riccati variable, coefficients arise from a linear algebraic system, and the organizer sign(m) separates solitary, rational, and periodic branches [44–46]. By contrast, the $(1/\Theta')$ expansion leverages a linear auxiliary ODE; regimes are organized by $\Delta = \vartheta^2 - 4\nu$, which cleanly splits non-oscillatory vs. oscillatory behavior, while the coefficients (A_0, A_1, A_2) directly control offset, steepening, and phase [46].

In this work, we provide a unified parameter-space classification of seven travelling-wave families for the improved Boussinesq equation. The generalized-tanh branch is organized by sign(m) (solitary

for $m < 0$, rational at $m = 0$, periodic for $m > 0$), while the $1/\Theta'$ branch is organized by $\Delta = \vartheta^2 - 4\nu$ (non-oscillatory for $\Delta > 0$, oscillatory for $\Delta < 0$). The coupled reduction is admissible when $1 - \mu\vartheta^2 > 0$, yielding $c = \kappa/\sqrt{1 - \mu\vartheta^2}$. Table 1 summarizes the regimes and the connecting limits; these closed forms are then used as manufactured benchmarks for the numerical validation.

Table 1. Summary of travelling-wave families and admissible sets.

Family	Defining constraint(s)	Qualitative type
ψ_1	$m < 0$	solitary ($\tanh^2$-type)
ψ_2	$m < 0$	solitary with poles ($\coth^2$-type)
ψ_3	$m = 0$	rational profile
ψ_4	$m > 0, \Delta < 0$	periodic, oscillatory ($\tan^2$-type)
ψ_5	$m > 0, \Delta > 0$	periodic, non-oscillatory ($\cot^2$-type)
ψ_6	$\Delta = \vartheta^2 - 4\nu$	$1/\Theta'$ branch; split by $\Delta \gtrless 0$
ψ_7	$1 - \mu\vartheta^2 > 0, c = \kappa/\sqrt{1 - \mu\vartheta^2}$	coupled admissible set

The overall paper structure is organized as follows. To begin with, Section 2 details the calculation of the IB equation's analytical traveling-wave solutions by systematic symbolic procedures. Subsequently, Section 3 outlines the numerical approach based on the Parabolic Monge-Ampère moving mesh method and also provides a detailed accuracy analysis together with an examination of the proposed scheme's stability characteristics. Finally, Section 4 includes a summary of the principal points and, in addition, highlights potential directions for the development of future research work, while Appendix A presents the explicit definition of the mesh-dependent operators appearing in the discretization.

2. Analytical solutions via traveling wave reductions

In this part, we utilize both the generalized tanh method and the $(1/\Theta')$-expansion method in order to find explicit traveling wave solutions of the IB equation. To begin with, we consider the nonlinear evolution equation

$$\mathcal{N}(\psi, \psi_t, \psi_x, \psi_{xx}, \psi_{tt}, \psi_{xxx}, \psi_{xxxx}, \dots) = 0, \tag{2.1}$$

where $\psi = \psi(x, t)$ is the dependent variable, x represents the space coordinate, t is time, and $\mathcal{N}(\cdot)$ represents a nonlinear differential operator.

Next, to find traveling wave solutions, we assume the transformation

$$\psi(x, t) = U(\xi), \quad \xi = x - ct, \tag{2.2}$$

with c being the wave speed. Consequently, the above substitution reduces the governing system to the ordinary differential form

$$\mathcal{M}(U, U_\xi, U_{\xi\xi}, U_{\xi\xi\xi}, U_{\xi\xi\xi\xi}, \dots) = 0, \tag{2.3}$$

where $\mathcal{M}(\cdot)$ is the transformed nonlinear operator. As a model case, we therefore take the IB Eq (1.1) in its traveling wave form:

$$c^2 U'' - \mu c^2 U'''' - \kappa^2 U'' - UU'' - (U')^2 = 0, \tag{2.4}$$

where the prime denotes differentiation with respect to ξ.

Next, by integrating (2.4) once with respect to ξ, and setting the integration constant to zero so as to remain consistent with vanishing-at-infinity boundary conditions, we obtain

$$c^2U' - \mu c^2U''' - \kappa^2U' - \tfrac{1}{2}(U^2)' = 0. \tag{2.5}$$

In (2.5), U''' constitutes the highest derivative term, whereas $(U^2)'$ represents the leading nonlinearity. To balance the degrees, we therefore assume $U \sim \Theta^N$ and $\Theta' \sim \Theta^2$, as suggested by the Riccati equation. Consequently, it follows that $U' \sim \Theta^{N+1}$, $U''' \sim \Theta^{N+3}$, and $(U^2)' \sim \Theta^{2N+1}$. By equating $N + 3 = 2N + 1$, we obtain $N = 2$. Hence, the solution is proposed in the form

$$U(\xi) = A_0 + A_1\Theta(\xi) + A_2\Theta^2(\xi), \tag{2.6}$$

where $\Theta(\xi)$ satisfies the Riccati equation

$$\Theta' = m + \Theta^2, \tag{2.7}$$

with m a constant parameter. The Riccati Eq (2.7) admits the solutions

$$\Theta(\xi) = \begin{cases} -\sqrt{-m}\,\tanh\Big(\sqrt{-m}\,(\xi-\xi_0)\Big), \quad \text{or } -\sqrt{-m}\,\coth\Big(\sqrt{-m}\,(\xi-\xi_0)\Big), & m<0,\\ -\dfrac{1}{\xi-\xi_0}, & m=0,\\ \sqrt{m}\,\tan\Big(\sqrt{m}\,(\xi-\xi_0)\Big), \quad \text{or } -\sqrt{m}\,\cot\Big(\sqrt{m}\,(\xi-\xi_0)\Big), & m>0. \end{cases} \tag{2.8}$$

where ξ_0 represents a phase shift.

Substituting expressions (2.6) and (2.7) into the reduced Eq (2.5), and collecting coefficients of Θ^k for $k = 0, 1, 2, 3, 4$, results in a system of algebraic equations. Solving this system yields

$$A_0 = \frac{A_2(8\mu m - 1)}{12\mu} - \kappa^2, \qquad A_1 = 0, \qquad c = \frac{\sqrt{-A_2}}{2\sqrt{3\mu}}. \tag{2.9}$$

To ensure a real wave speed c, the coefficient A_2 must have the opposite sign of μ. In particular, if $\mu > 0$, as in our model (1.1), then A_2 must be negative. As a final result, the solutions are classified by the sign of m as

$$\begin{aligned}
\psi_1(x,t) &= -\kappa^2 - A_2\left[m\tanh^2\Big(\sqrt{-m}\,(x-ct-\xi_0)\Big) + \frac{1}{12\mu} - \frac{2m}{3}\right], && m<0,\\
\psi_2(x,t) &= -\kappa^2 - A_2\left[m\coth^2\Big(\sqrt{-m}\,(x-ct-\xi_0)\Big) + \frac{1}{12\mu} - \frac{2m}{3}\right], && m<0,\\
\psi_3(x,t) &= -\kappa^2 - A_2\left[\frac{1}{12\mu} - \frac{1}{(x-ct-\xi_0)^2}\right], && m=0,\\
\psi_4(x,t) &= -\kappa^2 - A_2\left[-m\tan^2\Big(\sqrt{m}\,(x-ct-\xi_0)\Big) + \frac{1}{12\mu} - \frac{2m}{3}\right], && m>0,\\
\psi_5(x,t) &= -\kappa^2 - A_2\left[-m\cot^2\Big(\sqrt{m}\,(x-ct-\xi_0)\Big) + \frac{1}{12\mu} - \frac{2m}{3}\right], && m>0.
\end{aligned} \tag{2.10}$$

Direct substitution, in fact, confirms that all ψ_j satisfy (2.4) under the specified parameter relationships. Furthermore, the free parameters $(A_2, \kappa, \mu, m, \xi_0)$ determine key features of the solutions, namely amplitude, offset, dispersion, wave type, and phase positioning. Taken together, these closed-form solutions highlight the richness of wave structures admitted by Eq (1.1).

Figures 1 and 2 illustrate the hyperbolic solutions in (2.10). For $m < 0$, the solution ψ_1 represents a localized solitary pulse that translates rigidly with speed c from (2.9); here (A_2, μ) jointly determine the amplitude-dispersion balance, while κ fixes the baseline. In all cases considered, μ is positive, thereby ensuring a well-posed dispersive contribution. In addition, its companion ψ_2 exhibits the same translational invariance but with a sharper crest and near-pole steepening. Moreover, this solution possesses singularities at

$$x = ct + \xi_0 + \frac{n\pi i}{\sqrt{-m}}, \qquad n \in \mathbb{Z},$$

which arise from the poles of the coth function. In order to avoid plotting through these poles, the phase shift ξ_0 is used to control the visualization window. Both cases, therefore, anchor the $m < 0$ regime. Furthermore, in the limit $m \to 0^{\pm}$, the hyperbolic waves connect smoothly to the rational branch ψ_3 $(m = 0)$, which propagates without intrinsic periodicity and with algebraic tails. This limit, in turn, provides a natural link between solitary-like and periodic dynamics and thus serves as a convenient reference for comparison with numerical simulations. For $m > 0$, the trigonometric branches ψ_4 and ψ_5 produces periodic traveling wave trains with wave number $\sqrt{m}$ and period $\pi/\sqrt{m}$. The ψ_4 profile behaves like a lattice of peaks, whereas ψ_5 is phase-shifted with poles that can be eliminated by adjusting ξ_0. In these periodic cases, (A_2, κ) control offset and amplitude, while m governs spatial frequency.

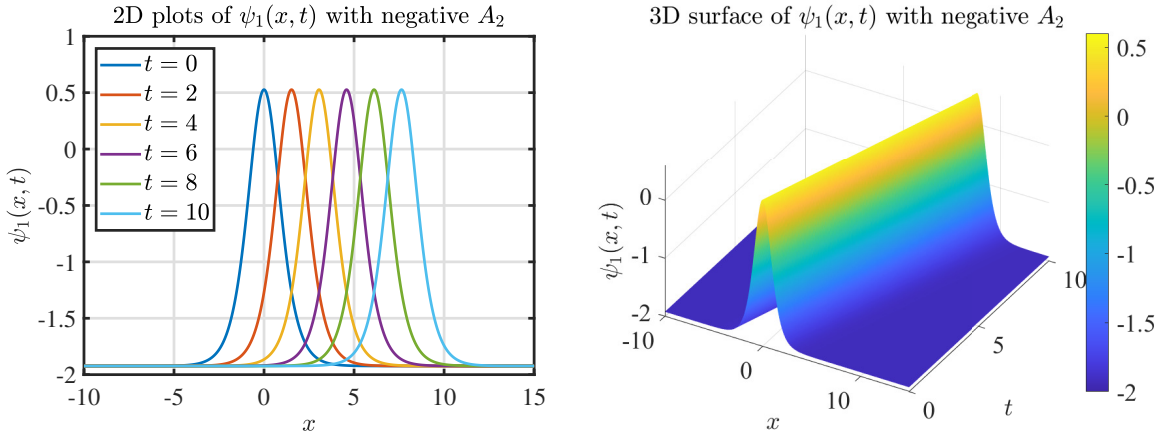

Figure 1. Analytical solution $\psi_1(x,t)$ obtained via the generalized tanh method with parameters $\kappa = 1.3$, $\mu = 0.5$, $m = -0.7$, $\xi_0 = 0$, and $A_2 = -3.5$. The left panel shows successive 2D profiles at $t = 0, 2, 4, 6, 8, 10$, while the right panel depicts the corresponding 3D surface.

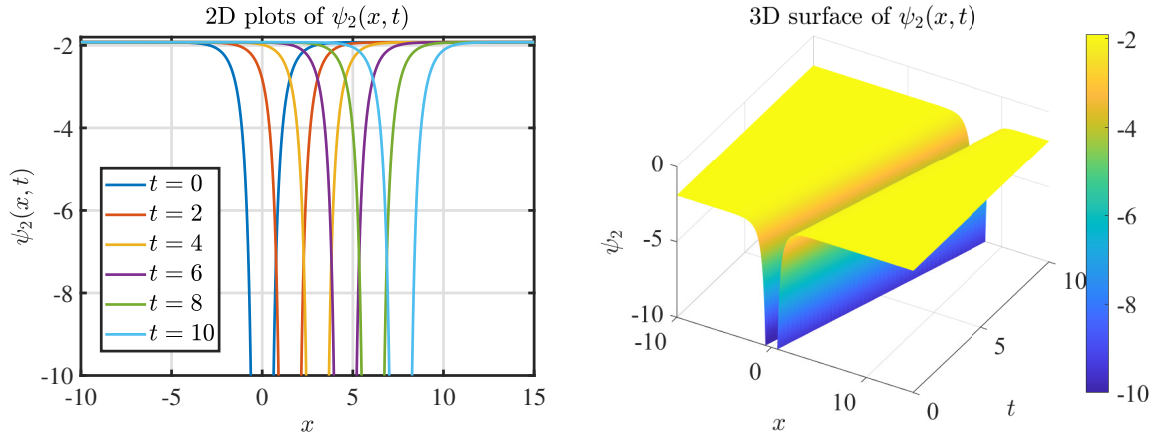

Figure 2. Analytical solution $\psi_2(x,t)$ with parameters $\kappa = 1.3$, $\mu = 0.5$, $m = -0.7$, $\xi_0 = 0$, and $A_2 = -3.5$. The left panel displays temporal slices from $t = 0$ to $t = 10$, while the right shows the full 3D surface.

Altogether, the set of functions ψ_1-ψ_5 therefore provides a continuous transition: Solitary-like for $m < 0$, rational for $m = 0$, and periodic for $m > 0$. Parameters regulate morphology and phase, while c consistently enforces rigid translation across all situations.

In place of the generalized tanh method, we now turn to the $(1/\Theta')$-expansion technique [46] in order to derive exact traveling-wave solutions. To this end, the proposed ansatz takes the form

$$U(\xi) = A_0 + A_1\left(\frac{1}{\Theta'(\xi)}\right) + A_2\left(\frac{1}{\Theta'(\xi)}\right)^2, \tag{2.11}$$

where A_0, A_1, and A_2 are constants to be determined.

Furthermore, the auxiliary function $\Theta(\xi)$ is required to satisfy the second-order linear differential equation

$$\Theta''(\xi) + \vartheta\,\Theta'(\xi) + \nu = 0, \tag{2.12}$$

with ϑ and ν taken as constant parameters. Consequently, the general solution to (2.12) reveals that $\Theta'(\xi)$ may exhibit exponential, hyperbolic, or trigonometric behavior, depending on the sign of $\vartheta^2 - 4\nu$.

In particular, one admissible form of the solution is

$$\Theta'(\xi) = b\,e^{-\vartheta\,\xi} - \frac{\nu}{\vartheta}, \tag{2.13}$$

where b denotes an integration constant.

By substituting the ansatz (2.11) together with its derivatives into the reduced Eq (2.5) and then collecting terms according to powers of $(1/\Theta'(\xi))$, we arrive at a system of algebraic equations. Solving this system in a straightforward manner consequently yields the following coefficient values:

$$A_0 = -\kappa^2 + \left(1 - \mu\vartheta^2\right)c^2, \qquad A_1 = -12\,\mu\,\nu\,c^2\,\vartheta, \qquad A_2 = -12\,\mu\,\nu^2\,c^2. \tag{2.14}$$

Therefore, a traveling wave solution to (2.5) can be expressed explicitly as

$$\psi_6(x,t) = -\kappa^2 + \left(1 - \mu\vartheta^2\right)c^2 - \frac{12\,\mu\,\nu\,c^2}{b\,e^{-\vartheta\,\xi} - \dfrac{\nu}{\vartheta}}\left(\vartheta + \frac{\nu}{b\,e^{-\vartheta\,\xi} - \dfrac{\nu}{\vartheta}}\right), \quad \xi = x - ct. \tag{2.15}$$

Figure 3 shows the traveling wave obtained through the $(1/\Theta')$-expansion method. In contrast to ψ_1–ψ_5, which arise from the generalized tanh method based on Riccati balance, this approach instead expands in powers of $1/\Theta'$, where Θ satisfies $\Theta'' + \vartheta\,\Theta' + \nu = 0$ with integration constant b. For the parameters used in the plots ($\kappa = 1.3$, $\mu = 0.5$, $\nu = -0.7$, $\vartheta = 0.8$, $b = 1$, $c = 1.5$) and time slices $t = 0{:}2{:}10$, the discriminant $\Delta = \vartheta^2 - 4\nu > 0$ accordingly places ψ_6 in the non-oscillatory branch. As a result, both panels display a single-peaked, shape-preserving pulse that propagates rigidly to the right with speed c. Moreover, the shape is dictated primarily by (ϑ, ν, b) rather than by the sign of m. Specifically, increasing ϑ steepens the leading edge, whereas changing ν sets the asymptotic level via the coefficients A_0, A_1, A_2, and the phase shift is instead governed by b. Furthermore, as $\Delta \to 0^+$, the profile approaches a critical exponential front; in contrast, for $\Delta < 0$, it bifurcates into oscillatory or periodic patterns that are qualitatively connected to the trigonometric wave trains ψ_4-ψ_5. In this way, ψ_6 completes the taxonomy of ψ_1-ψ_5: solitary-like for $m < 0$, rational for $m = 0$, and periodic for $m > 0$. Consequently, the $(1/\Theta')$-expansion provides an alternative reduction in which dispersion and phase are controlled by (ϑ, ν, b), while the rigid translation enforced by the traveling-wave ansatz is consistently retained, as evidenced by the aligned 2D sections and 3D surface.

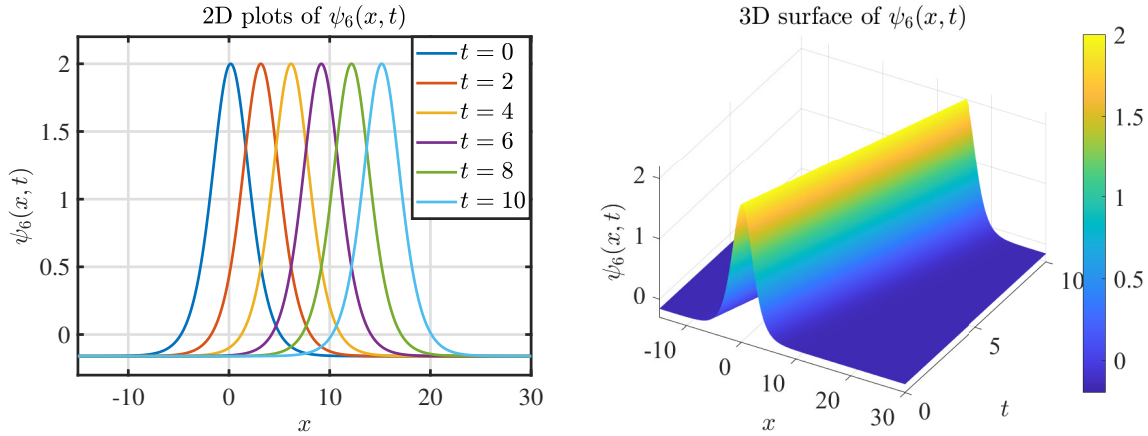

Figure 3. Analytical solution $\psi_6(x,t)$ obtained via the $(1/\Theta')$-expansion method (2.11)–(2.15). The left panel shows 2D time slices at $t = 0, 2, 4, 6, 8, 10$, and the right panel displays the corresponding 3D surface. For $\Delta = \vartheta^2 - 4\nu > 0$ (e.g., $\kappa = 1.3$, $\mu = 0.5$, $\vartheta = 0.8$, $\nu = -0.7$, $b = 1$, $c = 1.5$).

We now reformulate Eq (1.1) as a coupled system to lower the effective differential order and expose an auxiliary potential. In particular, the highest mixed term ψ_{xxtt} in $\psi_{tt} - \mu\,\psi_{xxtt} - \kappa^2\psi_{xx} - \psi\,\psi_{xx} - (\psi_x)^2 = 0$ is rewritten via $\psi_t = \phi_{xx}$ as $\psi_{xxtt} = \partial_{xx}(\psi_{tt}) = \partial_{xx}(\phi_{xxt})$, i.e., the time order drops from second to first while spatial operators remain. This yields a first integral in the travelling frame and makes the $(1/\Theta')$ ansatz algebraic and local. Numerically, the first-order in time form fits a BDF2 update, and the spatial operators stay centered and symmetric on the moving (PMA) mesh. Thus, the equivalent coupled system reads

$$\begin{aligned} &\psi_t = \phi_{xx}, \\ &\phi_{xxt} - \mu\,\phi_{xxxxt} - \kappa^2\,\psi_{xx} - \psi\,\psi_{xx} - (\psi_x)^2 = 0, \end{aligned} \tag{2.16}$$

and we accordingly introduce the travelling variables

$$\psi(x,t) = U(\xi), \quad \phi(x,t) = V(\xi), \quad \xi = x - ct.$$

Applying the $(1/\Theta')$-expansion to (2.16), together with the assumption $V(\xi) = A_0 + A_1/\Theta'(\xi)$ and the auxiliary condition $\Theta'' + \vartheta\Theta' + \nu = 0$, consequently yields

$$A_1 = \pm\frac{12\,\kappa^3\mu\nu}{(1-\mu\vartheta^2)^{3/2}}, \qquad c = \pm\frac{\kappa}{\sqrt{1-\mu\vartheta^2}}.$$

These relations, in turn, determine the coefficient A_1 and the wave speed c, and thus lead directly to explicit closed-form expressions for ψ and ϕ given below.

$$\begin{aligned} \psi_7(x,t) &= -\frac{12\,\kappa^2\mu\nu\,\vartheta^3\,b\,\exp\big(\vartheta\,[\,x \mp c\,t\,]\big)}{(1-\mu\vartheta^2)\Big(\vartheta\,b - \nu\,\exp(\vartheta\,[\,x\mp c\,t\,])\Big)^2}, \qquad c = \frac{\kappa}{\sqrt{1-\mu\vartheta^2}}, \\ \phi(x,t) &= A_0 \;\pm\; \frac{12\,\kappa^3\mu\nu}{(1-\mu\vartheta^2)^{3/2}\Big(b\,e^{-\vartheta\,[\,x\mp c\,t\,]} - \dfrac{\nu}{\vartheta}\Big)}, \end{aligned} \tag{2.17}$$

where A_0, b are integration constants.

Figures 4 and 5 display the coupled traveling pair obtained from the reformulation (2.16). Specifically, the component ψ_7 appears as a single-peaked pulse that travels rigidly with speed $c = \kappa/\sqrt{1-\mu\vartheta^2}$, as validated by the alignment of time slices. In this case, κ sets the base level, whereas the parameters (μ, ϑ, ν) govern the dispersion and steepening effects, and b defines the phase shift. Moreover, the companion potential ϕ is both monotonic and co-propagating, owing to the relation $\psi_t = \phi_{xx}$, which enforces identical propagation speed and synchronized level sets. Consequently, the pair (ψ_7, ϕ) embodies the order-reducing reformulation and uncovers a first-integral structure fully consistent with the $(1/\Theta')$ ansatz. These solution profiles, therefore, not only serve as analytical benchmarks but also provide naturally suited initial conditions for the subsequent numerical investigations. Finally, as the limit $1 - \mu\vartheta^2 \to 0^+$ is approached, the wavefront steepens considerably. At the same time, variations in ν translate into shifts in the asymptotic level, thereby affording precise control over waveform morphology and phase. The parameter–space structure of these regimes is concisely organized in Figure 6, which highlights how the travelling-wave families are partitioned according to the signs of m and Δ under the global admissibility condition $1 - \mu\vartheta^2 > 0$.

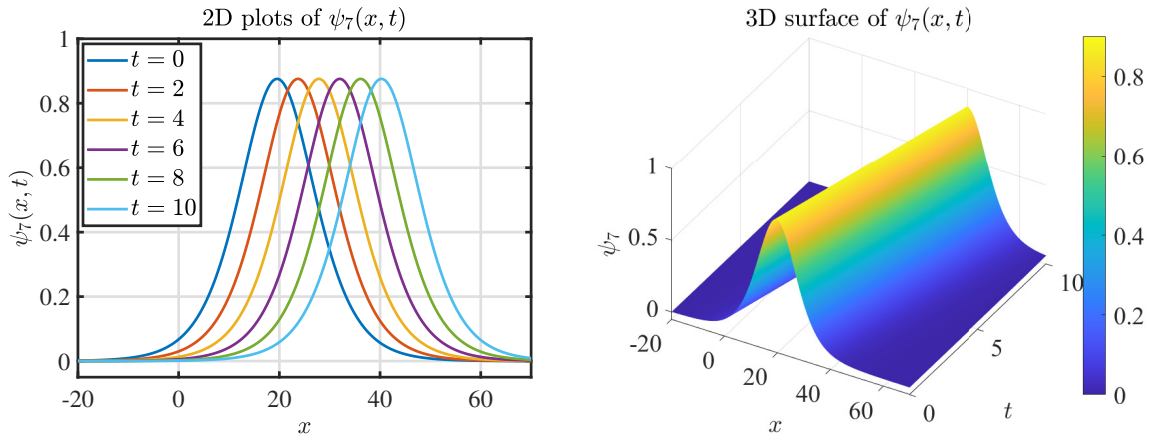

Figure 4. $\psi_7(x,t)$ from the coupled system (2.16) with $(\kappa, \mu, \vartheta, \nu, b, A_0, \xi_0) = (2,\ 1.7,\ -0.2,\ 1.0,\ 0.1,\ 0,\ 0)$. Left panel is 2D time slices at $t = 0{:}2{:}10$, and Right panel is a 3D surface.

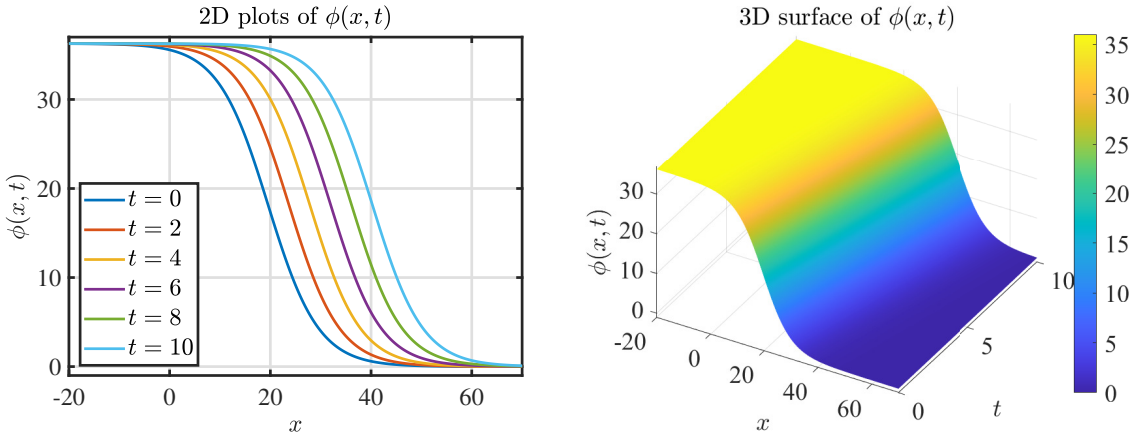

Figure 5. Associated potential $\phi(x,t)$ corresponding to ψ_7 in Figure 4 under the same parameters. Left panel is 2D time slices at t = 0:2:10, and Right panel is a 3D surface.

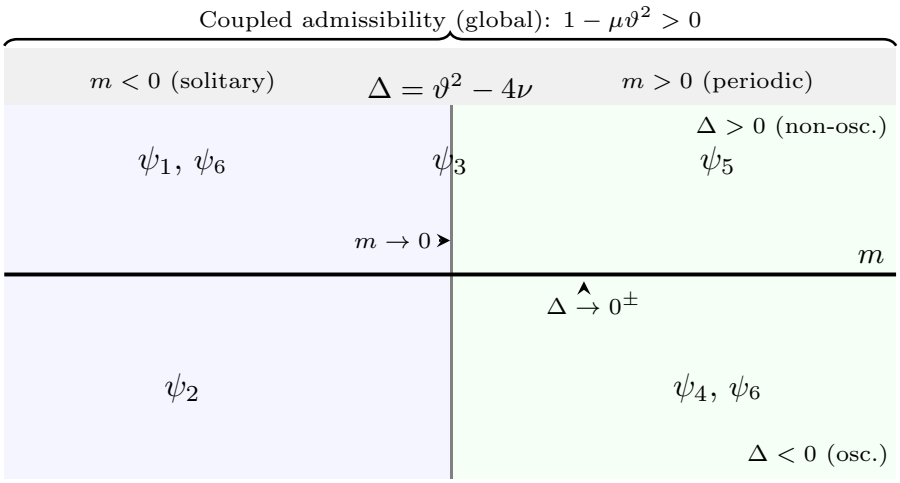

Figure 6. Parameter-space map for IBE travelling-wave families ψ_1–ψ_7. Shaded bands indicate $m < 0$, $m = 0$, and $m > 0$; the bold line $\Delta = 0$ separates oscillatory vs. non-oscillatory regimes. Family ψ_6 lies above/below according to $\Delta \gtrless 0$; ψ_7 satisfies the global condition $1 - \mu\vartheta^2 > 0$.

In conclusion, we highlight a structural aspect. We observe the conservative form of the IB Eq (1.1).

$$\partial_{tt}(\psi - \mu\,\psi_{xx}) \;-\; \partial_{xx}\Big(\kappa^2\psi + \tfrac{1}{2}\,\psi^2\Big) \;=\; 0, \tag{2.18}$$

since $\partial_{xx}(\frac{1}{2}\psi^2) = \psi_x^2 + \psi\,\psi_{xx}$. Define $A = \psi - \mu\psi_{xx}$ and $B = \kappa^2\psi + \frac{1}{2}\psi^2$; then $A_{tt} = B_{xx}$ by (2.18). Under periodic boundaries or vanishing to a constant background, the functionals

$$\mathcal{E}[\psi] = \tfrac{1}{2}\int_\Omega \Big((\psi_t - \mu\,\psi_{xxt})^2 + (\kappa^2\psi_x + \psi\,\psi_x)^2\Big)\,dx, \qquad \mathcal{P}[\psi] = \int_\Omega (\psi_t - \mu\,\psi_{xxt})(\kappa^2\psi_x + \psi\,\psi_x)\,dx$$

are conserved, since $\dfrac{d}{dt}\mathcal{E} = \int (A_t A_{tt} + B_x B_{xt})dx = [A_t B_x]_{\partial\Omega} = 0$ and $\dfrac{d}{dt}\mathcal{P} = \int (A_{tt}B_x + A_t B_{xt})dx = [\frac{1}{2}(B_x^2 + A_t^2)]_{\partial\Omega} = 0$. Also, for travelling waves $\psi(x,t) = U(\xi)$, $\xi = x - ct$, we obtain

$$c^2(U - \mu\,U'')'' - \Big(\kappa^2 U + \tfrac{1}{2}U^2\Big)'' = 0 \;\;\Rightarrow\;\; c^2(U - \mu\,U'') - \Big(\kappa^2 U + \tfrac{1}{2}U^2\Big) = A_1\,\xi + B_1.$$

Imposing vanishing far field (or periodic mean) yields $A_1 = B_1 = 0$. Thus, all travelling families ψ_1–ψ_7 given above are compatible with the conservative structure and possess all the invariants stated above under the same boundary setting.

3. Numerical framework via the parabolic Monge-Ampère method

Partial differential equations with sharp gradients or localized fine-scale features often require adaptive discretization in order to achieve both efficiency and accuracy [47]. Among the available adaptive strategies, the *r*-adaptive moving mesh approach is particularly effective because it redistributes existing grid points dynamically according to the evolving solution profile, without altering the total number of degrees of freedom. As a result, this relocation of mesh nodes concentrates resolution where it is most needed, thereby enabling accurate capture of steep gradients and localized structures at a significantly lower computational cost than uniform refinement.

Within the class of *r*-adaptive approaches, the Parabolic Monge-Ampère (PMA) method has proven especially effective [48]. In particular, it redistributes mesh nodes dynamically in time based on the evolving solution and thus can resolve multiple steep fronts or complex interfacial dynamics that would otherwise be prohibitively expensive on a fixed grid [49]. Moreover, in this framework, the mesh is constructed as the gradient of a scalar potential function, whose evolution is governed by a parabolic Monge-Ampère-type equation.

Hence, in this section, we detail the numerical framework of the PMA approach, introducing the mathematical formulation, methods of discretization, and realizations for practical use. We aim to show in detail how such a strategy provides an efficient and robust instrument for modeling wave phenomena in the models described above. Building on the general PMA framework described above, we now focus on its application to the IB equation, which features sharp traveling fronts and localized interactions on a smooth background. To effectively resolve these features, we implement *r*-adaptivity through PMA, where mesh nodes are drawn toward regions of high $|\psi_x|$ while preserving smoothness and quasi-uniformity of the map. This adaptivity improves phase accuracy and long-time fidelity and reduces dispersive overshoot relative to uniform meshes at the same DOF.

We solve the nonlinear ODE in Eq (2.5) in the travelling coordinate $\xi = x - ct$. We impose crest symmetry $U'(0) = 0$ and $U(0) = A$, where A is an amplitude parameter. We integrate the ODE with `ode45` on $[0, b]$ and adjust A with `fzero` so that the far-field condition at $\xi = b$ is met:

$$\left|U(b) - u_\infty\right| < \varepsilon,$$

where u_∞ is the constant background of the chosen travelling-wave family in (2.10). In zero-background cases, $u_\infty = 0$; otherwise, u_∞ equals the parameter-dependent level specified by that family. This ensures that the numerical profile matches the analytic travelling wave and decays smoothly toward its background. The resulting stationary profile $U(\xi)$ is then used as the initial condition for the time-dependent computation. In practice, we take b as the right boundary of the computational domain, use a small tolerance (e.g., $\varepsilon = 10^{-8}$), and advance in time with a BDF2 integrator (implemented via `ode15i`) with standard relative/absolute tolerances. Thus, all simulations start from data consistent with the steady solution of Eq (2.5).

To apply the PMA method to the IB system, the physical domain $[\alpha,\beta]$ is first mapped onto the fixed computational domain $[0, 1]$ via the time-dependent transformation

$$x = x(\eta, t) : [0, 1] \to [\alpha,\beta], \qquad t \geq 0,$$

where $\eta \in [0, 1]$ is the computational coordinate. Consequently, the dependent variables transform accordingly as

$$\tilde{\psi}(\eta, t) = \psi(x(\eta, t), t), \qquad \tilde{\phi}(\eta, t) = \phi(x(\eta, t), t). \tag{3.1}$$

Within the PMA framework, the mesh is subsequently generated from a scalar potential $P(\eta, t)$ through the relation

$$x(\eta, t) = P(\eta, t)_\eta,$$

subject to the boundary conditions

$$P(0, t) = \alpha, \qquad P(1, t) = \beta, \tag{3.2}$$

which ensures that the computational domain $[0, 1]$ is consistently mapped onto the physical domain $[\alpha,\beta]$. The time evolution of this potential is then governed by the one-dimensional PMA equation

$$\tau \left(I - \rho\, \partial_{\eta\eta}\right) \dot{P} = \omega(P_\eta, t)\, P_{\eta\eta}, \tag{3.3}$$

where $\tau > 0$ is a relaxation parameter controlling the rate of mesh adaptation, and $\rho \geq 0$ is a smoothing coefficient. Finally, the right-hand side involves the monitor function ω, which determines how strongly mesh points concentrate in different regions of the solution.

In this work, we adopt a gradient-based monitor function that depends on the variations of both dependent variables:

$$\omega(\psi, \phi) = \sqrt{1 + \frac{1}{P_{\eta\eta}^2}\left(\frac{\psi_\eta}{P_{\eta\eta}}\right)_\eta^2 + \frac{1}{P_{\eta\eta}^2}\left(\frac{\phi_\eta}{P_{\eta\eta}}\right)_\eta^2}. \tag{3.4}$$

Consequently, this form ensures that grid points cluster adaptively in regions where ψ or ϕ undergo rapid spatial variation, thereby enhancing the resolution of sharp gradients and localized structures.

However, to suppress oscillatory mesh movement and at the same time improve smoothness, the raw monitor (3.4) is subsequently replaced by a locally averaged version [52, 53]:

$$\hat{\omega}_j = \begin{cases} \frac{1}{3}\,(2\omega_1 + \omega_2), & j = 1, \\ \frac{1}{4}\,(\omega_{j-1} + 2\omega_j + \omega_{j+1}), & j = 2, \ldots, N_x, \\ \frac{1}{3}\,(\omega_{N_x} + 2\omega_{N_x+1}), & j = N_x + 1. \end{cases} \tag{3.5}$$

This smoothing step, therefore, prevents sudden mesh clustering near steep gradients and enhances the overall stability of the moving mesh algorithm.

Next, by applying the chain rule, spatial and temporal derivatives with respect to the physical coordinate x can be expressed in terms of the computational variable η and the mesh potential $P(\eta, t)$. Here, the notation $\dot{(\cdot)}$ denotes the partial derivative with respect to time t at fixed η. In particular, we obtain

$$\psi_x = \frac{\psi_\eta}{P_{\eta\eta}}, \qquad \psi_t = \dot{\psi} - \frac{\psi_\eta}{P_{\eta\eta}}\,\dot{P}_\eta, \qquad \phi_x = \frac{\phi_\eta}{P_{\eta\eta}}, \qquad \phi_t = \dot{\phi} - \frac{\phi_\eta}{P_{\eta\eta}}\,\dot{P}_\eta. \tag{3.6}$$

Subsequently, substituting these relations into the coupled IB system (2.16) introduced in Section 2,

$$\begin{aligned} \psi_t &= \phi_{xx}, \\ \varphi_{xxt} &= \kappa^2 \psi_{xx} + \psi\, \psi_{xx} + \psi_x^2, \\ \phi &= \varphi + \mu\, \phi_{xx}, \end{aligned} \tag{3.7}$$

and simplifying yields the transformed formulation in computational coordinates:

$$\begin{aligned} \dot{\psi} &= \frac{\psi_\eta}{P_{\eta\eta}}\, \dot{P}_\eta + \frac{1}{P_{\eta\eta}} \left(\frac{\phi_\eta}{P_{\eta\eta}} \right)_\eta, \\ \dot{\varphi} &= \frac{\varphi_\eta}{P_{\eta\eta}}\, \dot{P}_\eta + \kappa^2 \psi + \tfrac{1}{2} \psi^2, \\ \phi &= \varphi + \mu\, \frac{1}{P_{\eta\eta}} \left(\frac{\phi_\eta}{P_{\eta\eta}} \right)_\eta. \end{aligned} \tag{3.8}$$

Here, the auxiliary variable φ is finally introduced to reduce the highest-order mixed derivative, in line with the analytical formulation of Section 2.

The discrete mesh locations in physical space are obtained from the mesh potential as

$$x_j = \frac{P_{j+1} - P_{j-1}}{2\Delta_\eta}, \qquad j = 2, \ldots, N_x,$$

together with the boundary conditions $x_1 = \alpha$ and $x_{N_x+1} = \beta$. For initialization, the configuration is chosen as

$$P(\eta_j, 0) = \tfrac{1}{2} \eta_j^2, \qquad j = 1, \ldots, N_x + 1.$$

Subsequently, after applying central finite differences in the computational coordinate η, the semi-discrete form of (3.8) can be written compactly as

$$\begin{aligned} \dot{\psi}_j \;-\; \mathcal{A}_j(\psi, P)\, (\dot{P}_{j+1} - \dot{P}_{j-1}) \;&=\; \mathcal{B}_j(\phi, P), \\ \dot{\varphi}_j \;-\; C_j(\varphi, P)\, (\dot{P}_{j+1} - \dot{P}_{j-1}) \;&=\; \kappa^2 \psi_j \;+\; \tfrac{1}{2}\, (\psi^2)_j, \\ \varphi_j = \phi_j \;-\; \mathcal{B}_j(\phi, P), & \end{aligned} \tag{3.9}$$

where the mesh-dependent operators $\mathcal{A}_j$, $\mathcal{B}_j$, and C_j are given explicitly in Appendix A.

Starting from (3.9), time is advanced by a BDF2 formula. For any grid quantity $u^n \approx u(t^n)$ we use

$$D_t u^{n+1} \;=\; \frac{3u^{n+1} - 4u^n + u^{n-1}}{2\Delta t}, \qquad \dot{P}^{n+1} \;\approx\; \frac{P^{n+1} - P^n}{\Delta t}.$$

Hence, for $j = 2, \ldots, N_x$ the fully-discrete update reads (with the mesh fixed at the new time level and the operators assembled on P^{n+1}):

$$\begin{aligned} D_t \psi_j^{n+1} \;-\; \mathcal{A}_j(\psi^{n+1}, P^{n+1}) \left(\dot{P}_{j+1}^{n+1} - \dot{P}_{j-1}^{n+1} \right) \;&=\; \mathcal{B}_j(\phi^{n+1}, P^{n+1}), \\ D_t \varphi_j^{n+1} \;-\; C_j(\varphi^{n+1}, P^{n+1}) \left(\dot{P}_{j+1}^{n+1} - \dot{P}_{j-1}^{n+1} \right) \;&=\; \kappa^2 \psi_j^{n+1} \;+\; \tfrac{1}{2} (\psi^{n+1})_j^2, \end{aligned}$$

$$\varphi_j^{n+1} \;=\; \phi_j^{n+1} \;-\; \mathcal{B}_j(\phi^{n+1}, P^{n+1}),$$

while the mesh potential is advanced implicitly from (3.3) using the smoothed monitor (3.5):

$$\tau\,(I - \rho\,\delta_{\eta\eta})\,\frac{P^{n+1} - P^n}{\Delta t} \;=\; \widehat{\omega}^{n+1}\,\delta_{\eta\eta}P^{n+1}.$$

To validate the proposed numerical scheme, we present its implementation and the corresponding simulations. All computations were performed in MATLAB, which provides a convenient environment for scripting, visualization, and post-processing of the PMA moving-mesh algorithm [50, 51]. The implementation follows the semi-discrete formulation (3.9), coupled with the mesh evolution Eq (3.3) and the smoothed monitor (3.5). Unless stated otherwise, we use a BDF2 time integrator; in MATLAB, this is consistent with the implicit BDF family implemented in `ode15i`. Physical and numerical parameters are stated explicitly (domain, relaxation and smoothing coefficients, and initial mesh). This setup resolves steep gradients and localized structures reliably, forming the basis for the results reported below.

The 2D time slices of the solution variables for the parameter combination $\kappa = \mu = 1$ and relaxation parameter $\tau = 1$ are shown in Figure 7. Unless otherwise stated, the spatial domain is $[\alpha, \beta] = [-20, 70]$ with $N_x = 2001$ nodes, and time marching uses MATLAB stiff integrators suitable for the dispersive, weakly stiff regime of IB-type systems. The left panel shows a translating pulse of $\psi(x, t)$ moving without noticeable deformation along $t = 0{:}5{:}30$, and the right panel shows the corresponding monotone front of $\phi(x, t)$. The profiles are smooth and free of spurious oscillations over the simulation window, which indicates that the PMA discretization with $\tau = 1$ resolves the solution features at the chosen resolution.

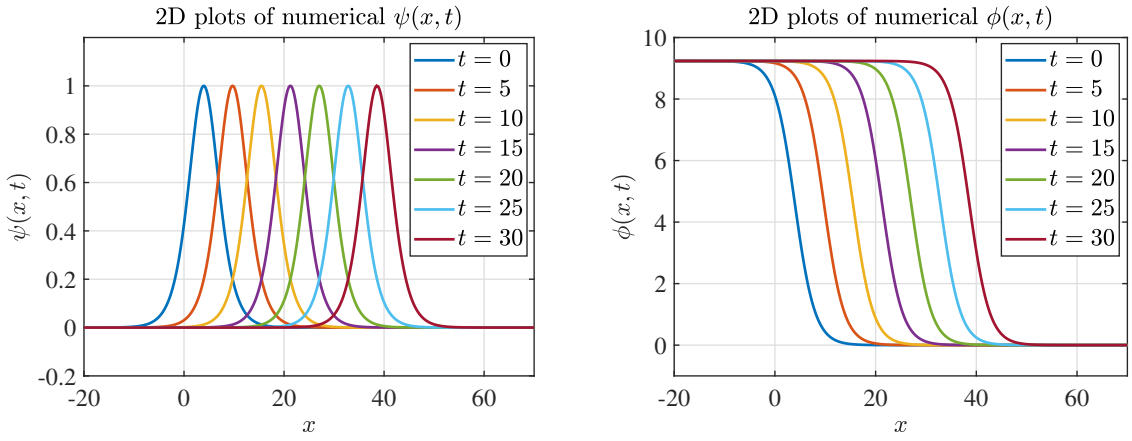

Figure 7. Numerical solutions of the IB system obtained using the PMA moving mesh method with parameters $\kappa = \mu = 1$ and relaxation parameter $\tau = 1$. The mesh consists of $N_x = 2001$ nodes over the spatial domain $[\alpha, \beta] = [-20, 70]$. The left panel shows the evolution of $\psi(x, t)$ at successive times $t = 0 : 5 : 30$, while the right panel displays the corresponding profiles of $\phi(x, t)$.

To study the grid motion, Figure 8 plots the mapping $x(\eta, t)$ of the computational coordinate η from the interval $[0, 1]$ into the physical coordinate x. As t increases, nodes cluster around sharp gradients

and spread in smooth regions, and the total number of degrees of freedom remains fixed. This *r*-adaptive property agrees with PMA theory [53] and prior observations for related PDEs, and it helps explain the absence of spurious dissipation in the baseline run.

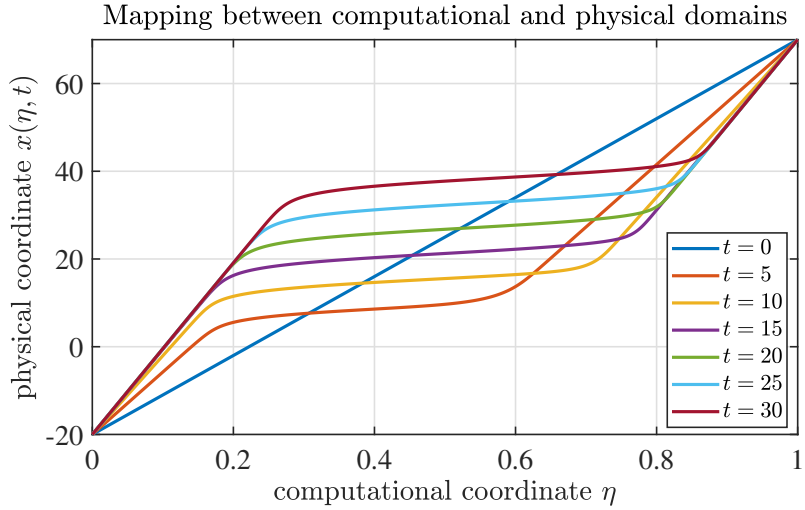

Figure 8. Mesh trajectory plot illustrating the mapping between the computational coordinate η and the physical coordinate $x(\eta, t)$. Simulation parameters are the same as in Figure 7. The trajectories illustrate how the adaptive mesh evolves in time to capture the solution dynamics.

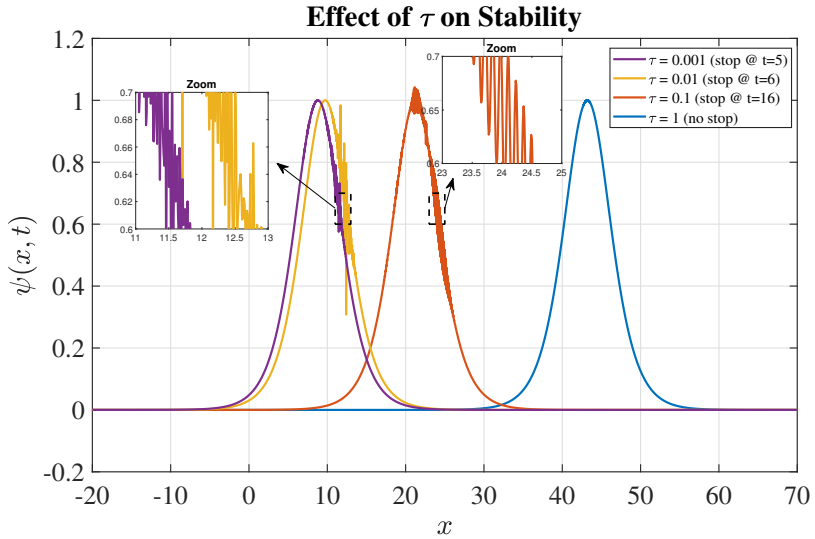

Figure 9. Effect of the relaxation parameter τ in the PMA moving-mesh method. Shown are snapshots of $\psi(x, t)$ for $\tau \in \{10^{-3}, 10^{-2}, 10^{-1}, 1\}$ using the same spatial resolution and domain as in Figure 7. Runs with $\tau = 10^{-3}$ and $\tau = 10^{-2}$ develop oscillations and terminate early (at $t \approx 5$ and $t \approx 6$), while $\tau = 10^{-1}$ remains stable until $t \approx 16$. The choice $\tau = 1$ sustains a smooth, stable evolution over the full-time interval. Insets magnify oscillatory windows for clarity.

We now examine the effect of τ on the stability and responsiveness of the mesh (Figure 9). As τ decreases, the mesh becomes more responsive under the monitor; however, it also increases the stiffness of the mesh PDE. In our problem, $\tau = 10^{-3}$ and $\tau = 10^{-2}$ cause ψ and the simulation to terminate early at $t \approx 5$ and $t \approx 6$ because the PDE is too stiff, respectively. A small $\tau = 10^{-1}$ enlarges the stable region, but the simulation still exits early at $t \approx 16$. By contrast, $\tau = 1$ is stable over the entire horizon. Thus, for the current IB configuration and monitor selection (3.5), a larger relaxation parameter provides a more stable balance between adaptivity and stability. We emphasize that this choice depends on the problem and should be adjusted together with the monitor smoothing and the time-step control.

Overall, the MATLAB PMA concentrates resolution around evolving features with a predetermined number of nodes and solves the IB dynamics automatically. Stable long-term integration holds for the default setting ($\tau = 1$), and for small τ the meshes are more reactive at the cost of stiffness and visible oscillations. These results align with recommendations tested in the moving-mesh literature [53, 54] and offer practical defaults for future parameter studies.

3.1. Accuracy and stability of the PMA scheme

The semi-discrete formulation obtained from the PMA transformation preserves the second-order spatial accuracy of central finite differences in the computational variable η. Time integration is carried out with the two-step backward differentiation formula (BDF2), yielding a second-order scheme in both space and time under mesh regularity.

Let $\Delta\eta = 1/N_x$ and Δt denote the spatial and temporal step sizes, with the Jacobian $J(\eta, t) = P_{\eta\eta}$. A Taylor expansion gives the local truncation error

$$T \;=\; O(\Delta\eta^2) + O(\Delta t^2) + O(\Delta\eta^2\,\|J_\eta\|_\infty) + O(\Delta t^2\,\|\dot{J}\|_\infty),$$

showing that additional terms are proportional to mesh variations. Provided that J remains bounded and smooth, the fully discrete solution satisfies

$$\|\psi - \psi_h\| + \|\phi - \phi_h\| \;=\; O(\Delta\eta^2 + \Delta t^2).$$

Convergence is verified numerically by refining $\Delta\eta$ and Δt with proportional scaling and monitoring errors in L^2 norms, together with mesh-quality indicators such as $\|J_\eta\|_\infty$ and $J_{\min}$. Thus, the numerical scheme achieves the same nominal order as fixed-mesh discretizations while concentrating resolution adaptively in regions of interest.

Table 2 reports the relative L_2 error at $t = 30$ on the fixed domain $[\alpha, \beta] = [-20, 70]$ while taking N_x as the only variable; to avoid an interpolation bias, the exact traveling profile is evaluated on the adaptive nodes. Clearly, the error monotonically decreases while N_x increases. The corresponding log-log trend is displayed in Figure 10. The fitted slope is about 1.95 and fairly close to the reference slope of 2. Hence, the expected second-order spatial accuracy is achieved by the adaptive PMA discretization. Moreover, fewer degrees of freedom than those required on a uniform mesh are sufficient to attain a given target accuracy.

Table 2. Adaptive mesh errors at $t = 30$ on the fixed domain $[\alpha, \beta] = [-20, 70]$.

N_x	Relative L_2
200	1.85×10^{-2}
400	5.12×10^{-3}
800	1.01×10^{-3}
1600	2.6×10^{-4}
3200	7.73×10^{-5}

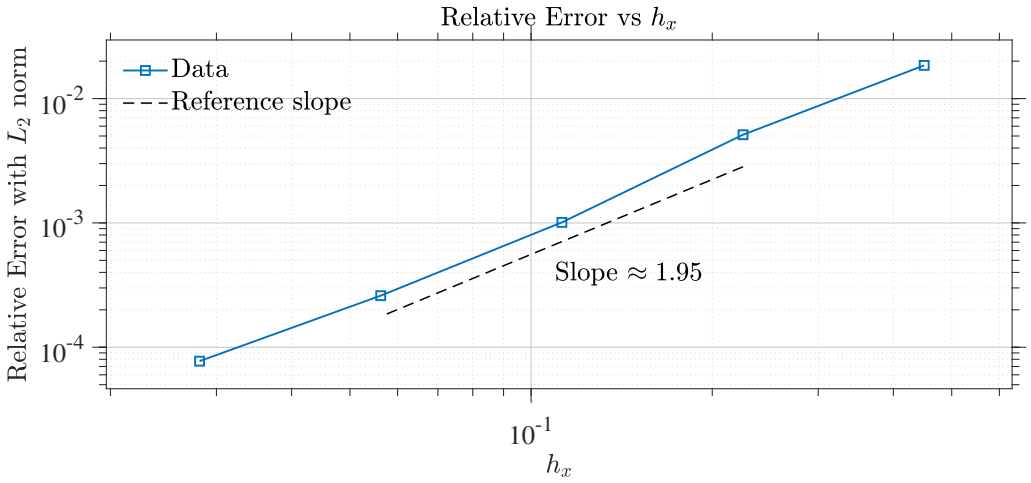

Figure 10. Log-log plot of the relative L_2 error vs. spatial step h_x at $t = 30$ on $[\alpha, \beta] = [-20, 70]$. Exact data are sampled on the adaptive nodes. Markers correspond to $N_x \in \{200, 400, 800, 1600, \text{and } 3200\}$. The observed slope ≈ 1.95 confirms second-order accuracy.

The stability of the proposed scheme is governed by both the time discretization and the mesh dynamics. Since the temporal integration is carried out with BDF2, the method is A-stable for all eigenvalues with negative real parts for the linearized problem on a fixed mesh. When the mesh evolves according to the parabolic Monge-Ampère Eq (3.3), additional coefficients depending on $\dot{P}_\eta$ appear, but they do not compromise the A-stability of BDF2 as long as the mesh remains sufficiently smooth [55].

A von Neumann analysis on a frozen mesh ($J = P_{\eta\eta} = \text{const.}$) yields an amplification factor $G(\xi)$ with $|G(\xi)| \leq 1$ for all Fourier modes ξ, confirming linear stability on fixed meshes. For a moving mesh, stability reduces to mesh regularity, i.e.,

$$0 < J_{\min} \leq J(\eta, t) \leq J_{\max} < \infty, \qquad \text{with} \quad \|\dot{J}\|_\infty < \infty,$$

so that the coupled PMA-BDF2 scheme inherits the stability of the underlying fixed-mesh discretization. In practice, long-time experiments confirm the absence of spurious oscillations provided the smoothing procedure (3.5) is applied and the relaxation parameter τ in (3.3) is chosen moderately.

Overall, the combined effect of accuracy and stability guarantees convergence of the PMA-based discretization, since consistency bounds the local truncation error while stability prevents its growth in time, thereby enforcing

$$\|e_h\| \to 0 \qquad \text{as } \Delta\eta, \Delta t \to 0.$$

4. Conclusions

In the present work, we explored the Improved Boussinesq model through both analytical reductions the adaptive numerical solutions. Upon applying the generalized tanh method and the $(1/\Theta')$-expansion method, an enriched family of closed-form traveling-wave solutions ensued, encompassing solitary, rational, and periodic configurations. These solutions were employed as strict benchmarks for the verification of the adaptive moving mesh discretization. In the numerical arena, implicit finite differences coupled with the Parabolic Monge-Ampère method accurately captured solitary interactions and steep gradients with second-order accuracy and long-time stability. The results reflect the effectiveness of adaptive redistributions of the mesh for the minimization of the computational cost at the expense of an overall preservation of accuracy. Beyond yielding numerical reliability and analytical insight, the paper showcases the increased accessibility of adaptive strategies for the more general category of nonlinear dispersive PDEs within the fields of hydrodynamics, elasticity, and optics. Future applications can expand the framework presented herein toward multidimensional spaces, more rigorous-looking boundary conditions, and coupled nonlinear sets to further promote the description of nonlinear wave phenomena through the numerical simulation of PDE models.

Author contributions

Amer Ahmed: Conceptualization, methodology, formal analysis, validation, writing original draft; Taghread Ghannam Alharbi: Investigation, validation; A. R. Alharbi: Conceptualisation, investigation, data curation, visualisation; Ishak Hashim: Supervision, writing review and editing. All authors have read and approved the final version of the manuscript for publication.

Use of Generative-AI tools declaration

The authors declare that they did not use artificial intelligence (AI) tools to create this article.

Acknowledgments

The author, Amer Ahmed, is grateful to Taibah University for its generous support in the form of a fully paid scholarship, which significantly helped in successfully completing this work.

Conflict of interest

The authors declare no conflicts of interest.

References

1. I. L. Bogolubsky, Some examples of inelastic soliton interaction, *Comput. Phys. Commun.*, **13** (1977), 149–155. https://doi.org/10.1016/0010-4655(77)90009-1
2. V. S. Manoranjan, A. R. Mitchell, J. Ll. Morris, Numerical solutions of the good Boussinesq equation, *SIAM J. Sci. Stat. Comput.*, **5** (1984), 946–957. https://doi.org/10.1137/0905065

3. L. Debnath, Nonlinear diffusion-reaction phenomena, In: *Nonlinear partial differential equations for scientists and engineers*, Birkhäuser Boston, 2012. https://doi.org/10.1007/978-0-8176-8265-1_8
4. Z. Yang, B. Y. C. Hon, An improved modified extended tanh-function method, *Z. Naturforsch.*, **61a** (2006), 103–115. https://doi.org/10.1515/zna-2006-3-401
5. Y. Li, Trial equation method for solving the improved Boussinesq equation, *Adv. Pure Math.*, **4** (2014), 47–52. https://doi.org/10.4236/apm.2014.42007
6. B. Wongsaijai, C. Oonariya, K. Poochinapan, Compact structure-preserving algorithm with high accuracy extended to the improved Boussinesq equation, *Math. Comput. Simul.*, **178** (2020), 125–150. https://doi.org/10.1016/j.matcom.2020.05.002
7. M. A. Kawser, M. A. Akbar, M. A. Khan, H. A. Ghazwani, Exact soliton solutions and the significance of time-dependent coefficients in the Boussinesq equation: Theory and application in mathematical physics, *Sci. Rep.*, **14** (2024), 762. https://doi.org/10.1038/s41598-023-50782-1
8. Chapter 2 properties of the 2-D system of Shallow-Water Equations (2-D SSWE), In: *Elsevier oceanography series*, **55** (1992), 60–106. https://doi.org/10.1016/S0422-9894(08)70156-9
9. R. B. Hetnarski, J. Ignaczak, *The mathematical theory of elasticity*, Boca Raton: CRC Press, 2011. https://doi.org/10.1201/9781439828892
10. O. Darrigol, Joseph Boussinesq's legacy in fluid mechanics, *C. R. Mécanique*, **345** (2017), 427–445. https://doi.org/10.1016/j.crme.2017.05.008
11. S. Ibrahim, T. A. Sulaiman, A. Yusuf, D. U. Ozsahin, D. Baleanu, Wave propagation to the doubly dispersive equation and the improved Boussinesq equation, *Opt. Quant. Electron.*, **56** (2024), 20. https://doi.org/10.1007/s11082-023-05571-5
12. M. Iqbal, W. A. Faridi, M. Alammari, F. A. H. Alomari, N. E. Alsubaie, S. Ibrahim, et al., Dynamical analysis of optical soliton structures for wave propagation in nonlinear low-pass electrical transmission lines under effective approach, *Opt. Quant. Electron.*, **56** (2024), 1036. https://doi.org/10.1007/s11082-024-06664-5
13. B. Karaagac, Y. Ucar, A. Esen, Dynamics of modified improved Boussinesq equation via Galerkin finite element method, *Math. Method. Appl. Sci.*, **43** (2020), 10204–10220. https://doi.org/10.1002/mma.6687
14. M. Bilal, J. Ren, A. S. A. Alsubaie, K. H. Mahmoud, M. Inc, Dynamics of nonlinear diverse wave propagation to Improved Boussinesq model in weakly dispersive medium of shallow waters or ion acoustic waves using efficient technique, *Opt. Quant. Electron.*, **56** (2024), 21. https://doi.org/10.1007/s11082-023-05587-x
15. W. L. Lee, Z. Tan, Moving mesh methods for Boussinesq equation, *Int. J. Numer. Meth. Fl.*, **61** (2009), 1161–1178. https://doi.org/10.1002/fld.2008
16. M. A. E. Abdelrahman, M. B. Almatrafi, A. Alharbi, Fundamental solutions for the coupled KdV system and its stability, *Symmetry*, **12** (2020), 429. https://doi.org/10.3390/sym12030429
17. S. A. Khuri, A complex tanh-function method applied to nonlinear equations of Schrödinger type, *Chaos Soliton. Fract.*, **20** (2004), 1037–1040. https://doi.org/10.1016/j.chaos.2003.09.042

18. A. M. Wazwaz, The extended tanh method for abundant solitary wave solutions of nonlinear wave equations, *Appl. Math. Comput.*, **187** (2007), 1131–1142. https://doi.org/10.1016/j.amc.2006.09.013

19. J. Manafian, J. Jalali, A. Alizadehdiz, Some new analytical solutions of the variant Boussinesq equations, *Opt. Quant. Electron.*, **50** (2018), 80. https://doi.org/10.1007/s11082-018-1345-z

20. M. Ozisik, A. Secer, M. Bayram, A. Yusuf, T. A. Sulaiman, Soliton solutions of the Boussinesq equation via an efficient analytical technique, *Mod. Phys. Lett. B*, **36** (2022), 2250149. https://doi.org/10.1142/S0217984922501494

21. A. Aasaraai, The application of modified F-expansion method solving the Maccari's system, *J. Adv. Math. Comput. Sci.*, **11** (2015), 1–14. https://doi.org/10.9734/BJMCS/2015/19938

22. S. K. Mohanty, O. V. Kravchenko, A. N. Dev, Exact traveling wave solutions of the Schamel Burgers' equation by using generalized-improved and generalized G′/G expansion methods, *Results Phys.*, **33** (2022), 105124. https://doi.org/10.1016/j.rinp.2021.105124

23. M. A. E. Abdelrahman, A. Alharbi, Analytical and numerical investigations of the modified Camassa-Holm equation, *Pramana J. Phys.*, **95** (2021), 117. https://doi.org/10.1007/s12043-021-02153-6

24. A. G. Bratsos, A second order numerical scheme for the improved Boussinesq equation, *Phys. Lett. A*, **370** (2007), 145–147. https://doi.org/10.1016/j.physleta.2007.05.050

25. Z. Zhang, F. Lu, Quadratic finite volume element method for the improved Boussinesq equation, *J. Math. Phys.*, **53** (2012), 013505. https://doi.org/10.1063/1.3672197

26. Z. Ming, B. Teng, S. X. Liu, Numerical simulation of improved Boussinesq equations by a finite element method, *J. Hydrodyn.*, **15** (2003), 31–40.

27. C. Zhang, J. Huang, C. Wang, X. Yue, On the operator splitting and integral equation preconditioned deferred correction methods for the "good" Boussinesq equation, *J. Sci. Comput.*, **75** (2018), 687–712. https://doi.org/10.1007/s10915-017-0552-2

28. A. Ahmed, A. R. Alharbi, H. S. Alayachi, I. Hashim, Exact and numerical approaches for solitary and periodic waves in a (2+1)-dimensional breaking soliton system with adaptive moving mesh, *AIMS Math.*, **10** (2025), 8252–8276. https://doi.org/10.3934/math.2025380

29. A. Ahmed, A. R. Alharbi, I. Hashim, Exact and numerical solutions of the generalized breaking soliton system: Insights into non-linear wave dynamics, *AIMS Math.*, **10** (2025), 5124–5142. https://doi.org/10.3934/math.2025235

30. C. J. Budd, J. F. Williams, Moving mesh generation using the parabolic Monge-Ampère equation, *SIAM J. Sci. Comput.*, **31** (2009), 3438–3465. https://doi.org/10.1137/080716773

31. A. R. Alharbi, Numerical solutions to two-dimensional fourth order parabolic thin film equations using the Parabolic Monge-Ampère method, *AIMS Math.*, **8** (2023), 16463–16478. https://doi.org/10.3934/math.2023841

32. M. H. M. Sulman, T. B. Nguyen, R. D. Haynes, W. Huang, Domain decomposition parabolic Monge-Ampère approach for fast generation of adaptive moving meshes, *Comput. Math. Appl.*, **84** (2021), 97–111. https://doi.org/10.1016/j.camwa.2020.12.007

33. C. J. Budd, W. Huang, R. D. Russell, Adaptivity with moving grids, *Acta Numer.*, **18** (2009), 111–241. https://doi.org/10.1017/S0962492906400015

34. A.-M. Wazwaz, The tanh method for traveling wave solutions of nonlinear equations, *Appl. Math. Comput.*, **154** (2004), 713–723. https://doi.org/10.1016/S0096-3003(03)00745-8

35. H. Q. Sun, A. H. Chen, Exact solutions of the classical Boussinesq system, *Arab J. Basic Appl. Sci.*, **25** (2018), 85–91. https://doi.org/10.1080/25765299.2018.1449416

36. A. R. Seadawy, D. Lu, C. Yue, Travelling wave solutions of the generalized nonlinear fifth-order KdV water wave equations and its stability, *J. Taibah Univ. Sci.*, **11** (2017), 623–633. https://doi.org/10.1016/j.jtusci.2016.06.002

37. W. O. Apeanti, D. Lu, H. Zhang, D. Yaro, S. W. Akuamoah, Traveling wave solutions for complex nonlinear space-time fractional order (2+1)-dimensional Maccari dynamical system and Schrödinger equation with dual power law nonlinearity, *SN Appl. Sci.*, **1** (2019), 530. https://doi.org/10.1007/s42452-019-0537-x

38. L. Li, E. Li, M. Wang, The (G'/G, 1/G)-expansion method and its application to travelling wave solutions of the Zakharov equations, *Appl. Math. J. Chin. Univ.*, **25** (2010), 454–462. https://doi.org/10.1007/s11766-010-2128-x

39. M. A. E. Abdelrahman, E. H. M. Zahran, M. M. A. Khater, The exp(-$\phi(\xi)$)-expansion method and its application for solving nonlinear evolution equations, *Int. J. Mod. Nonlinear Theor. Appl.*, **4** (2015), 37–47. https://doi.org/10.4236/ijmnta.2015.41004

40. A. R. Alharbi, *Numerical solution of thin-film flow equations using adaptive moving mesh methods*, 2016. Available from: `https://keele-repository.worktribe.com/output/407075`.

41. A. R. Alharbi, Numerical investigation for the GRLW equation using Parabolic Monge Ampere equation, *Int. J. Math. Comput. Sci.*, **15** (2020), 443–462.

42. A. R. Alharbi, A Study of traveling wave structures and numerical investigation of two-dimensional Riemann problems with their stability and accuracy, *CMES-Comp. Model. Eng.*, **134** (2023), 2193–2209. https://doi.org/10.32604/cmes.2022.018445

43. M. B. Almatrafi, A. R. Alharbi, A. R. Seadawy, Structure of analytical and numerical wave solutions for the Ito integro-differential equation arising in shallow water waves, *J. King Saud Univ. Sci.*, **33** (2021), 101375. https://doi.org/10.1016/j.jksus.2021.101375

44. E. Fan, Y. C. Hona, Generalized tanh method extended to special types of nonlinear equations, *Z. Naturforsch. A*, **57** (2002), 692–700. https://doi.org/10.1515/zna-2002-0809

45. T. G. Alharbi, A. Alharbi, A study of traveling wave structures and numerical investigations into the coupled nonlinear Schrödinger equation using advanced mathematical techniques, *Mathematics*, **11** (2023), 4597. https://doi.org/10.3390/math11224597

46. K. K. Ali, R. Yilmazer, A. Yokus, H. Bulut, Analytical solutions for the (3+1)-dimensional nonlinear extended quantum Zakharov-Kuznetsov equation in plasma physics, *Physica A*, **548** (2020), 124327. https://doi.org/10.1016/j.physa.2020.124327

47. L. F. Diachin, R. Hornung, P. Plassmann, A. Wissink, Parallel adaptive mesh refinement, In: *Parallel processing for scientific computing*, 2006, 143–162. https://doi.org/10.1137/1.9780898718133.ch8

48. P. A. Browne, C. J. Budd, C. Piccolo, M. Cullen, Fast three dimensional r-adaptive mesh redistribution, *J. Comput. Phys.*, **275** (2014), 174–196. https://doi.org/10.1016/j.jcp.2014.06.009

49. C. J. Budd, J. F. Williams, Parabolic Monge-Ampère methods for blow-up problems in several spatial dimensions, *J. Phys. A Math. Gen.*, **39** (2006), 5425–5449. https://doi.org/10.1088/0305-4470/39/19/S06

50. L. F. Shampine, Solving $0 = F(t, y(t), y'(t))$ in matlab, *J. Numer. Math.*, **10** (2002), 291–310. https://doi.org/10.1515/JNMA.2002.291

51. A. Alharbi, S. Naire, An adaptive moving mesh method for thin film flow equations with surface tension, *J. Comput. Appl. Math.*, **319** (2017), 365–384. https://doi.org/10.1016/j.cam.2017.01.019

52. T. Tang, Moving mesh methods for computational fluid dynamics, *Contemp. Math.*, **383** (2005), 141–173.

53. W. Huang, R. D. Russell, Variational mesh adaptation methods, In: *Adaptive moving mesh methods*, New York: Springer, 2011. https://doi.org/10.1007/978-1-4419-7916-2_6

54. C. Lu, W. Huang, J. Qiu, An adaptive moving mesh finite element solution of the regularized long wave equation, *J. Sci. Comput.*, **74** (2018), 122–144. https://doi.org/10.1007/s10915-017-0427-6

55. E. Hairer, G. Wanner, *Solving ordinary differential equations II: Stiff and differential-algebraic problems*, Berlin: Springer, 1996. https://doi.org/10.1007/978-3-642-05221-7

Appendix

A. Definitions of the mesh-dependent operators

This appendix provides the explicit forms of the operators introduced in (3.9). They depend nonlinearly on the mesh potential $P(\eta, t)$ and its discrete derivatives. For interior indices m, we define

$$\begin{aligned} \mathcal{A}_m(\psi, P) &= \frac{\psi_{m+1} - \psi_{m-1}}{P_{m+2} - 2P_m + P_{m-2}}, \\ D_m(\phi, P) &= \frac{\phi_{m+1} - \phi_m}{P_{m+2} - P_{m+1} - P_m + P_{m-1}}, \\ \mathcal{B}_m(\phi, P) &= \frac{8\,\Delta_\eta^2}{P_{m+2} - 2P_m + P_{m-2}}(D_m - D_{m-1}), \\ C_m(\varphi, P) &= \frac{\varphi_{m+1} - \varphi_{m-1}}{P_{m+2} - 2P_m + P_{m-2}}. \end{aligned} \tag{A.1}$$

These definitions make the semi-discrete scheme in (3.9) fully reproducible while keeping the main text concise. They follow directly from the coordinate transformation and the application of central finite difference stencils in the computational coordinate.